






Analysis

Fatty acid metabolism-related risk signature revealing the immune landscape of neuroblastoma and predicting overall survival in pediatric neuroblastoma patients

Shizun Wang¹  · Dan Zhang²  · Ming Ge³ · Nijia Zhang³ · Wei Yang³  · Yuqin Liu¹ 

Received: 4 September 2024 / Accepted: 24 April 2025

Published online: 13 May 2025

© The Author(s) 2025 

Abstract

Background Tumor metabolic reprogramming is a hallmark in cancer cells, wherein fatty acid metabolism assumes a pivotal role in energy supply and the provision of diverse biosynthetic precursors. However, there is a lack of systematic analysis regarding the impact of fatty acid metabolism on prognosis in neuroblastoma (NB) patients and its influence on the immune microenvironment.

Methods We acquired RNA expression profiles and corresponding clinical-pathological information for NB patients from the Gene Expression Omnibus, ArrayExpress, and TARGET databases. The GSE49710 cohort was utilized as a training set, whereas E-MTAB-8248 and the TARGET cohorts served as testing sets. Consensus clustering was employed to identify molecular subtypes based on fatty acid metabolism. Independent prognostic genes were pinpointed using LASSO-Cox analysis, which facilitated the development of a novel risk signature that was subsequently validated using the testing sets. We then proceeded to analyze the predictive power of the risk signature for prognosis, its correlation with clinical-pathological features, the immune landscape, and drug sensitivity.

Results In the consensus clustering analysis, patients in the training set were segregated into two clusters. Cluster 2 exhibiting significantly poorer overall survival (OS) compared to cluster 1. Moreover, cluster 2 was markedly associated with clinical-pathological features indicative of poor prognosis. Following this, univariate Cox regression analysis revealed 207 fatty acid metabolism genes (FMGs) correlated with patient OS. A risk signature based on 35 FMGs was constructed using LASSO-Cox regression analysis, demonstrating significant predictive accuracy and discrimination in both the training and testing sets. The risk signature emerged as an independent prognostic factor and was integrated with multiple clinical-pathological features to develop a nomogram. In the immune landscape analysis, the high-risk group displayed a compromised antigen presentation mechanism, reduced infiltration levels of various immune cells, and escaping of CD8+ T cells and NK cells. Additionally, different risk groups could exhibit different responsiveness to immune checkpoint inhibitors. Lastly, potential chemotherapeutic agents for each risk group were predicted.

Conclusion The novel risk signature, derived from FMGs, demonstrated promising efficacy in predicting the prognosis of NB patients, elucidating their immune landscape, and guiding therapeutic strategies.

Supplementary Information The online version contains supplementary material available at <https://doi.org/10.1007/s12672-025-02479-2>.

✉ Yuqin Liu, liuyuqin@pumc.edu.cn; Shizun Wang, shizunwang@163.com; Dan Zhang, zhangdan7006@163.com; Ming Ge, geming88@126.com; Nijia Zhang, zoro1992612@163.com; Wei Yang, dr.yangwei@foxmail.com | ¹Department of Pathology, Cell Resource Center, Institute of Basic Medical Sciences, Chinese Academy of Medical Sciences (CAMS) and School of Basic Medicine, Peking Union Medical College (PUMC), Beijing, China. ²Beijing Cygenta BioTechnology Co., Ltd, Beijing, China. ³Department of Neurosurgery, National Center for Children's Health, Beijing Children's Hospital, Capital Medical University, Beijing, China.



Keywords Neuroblastoma · Fatty acid metabolism genes (FMGs) · Prognosis · Drug sensitivity · Immune landscape

1 Introduction

Neuroblastoma (NB), a common extracranial solid tumor in children, originates from undifferentiated neural crest cells and can occur anywhere within the sympathetic nervous system [1]. Despite comprising only 6%–15% of all childhood malignancies [2, 3], it accounts for approximately 15% of all childhood cancer-related deaths [4]. The disease is characterized by significant heterogeneity at the genetic, clinical, and therapeutic response levels. Some tumors spontaneously regress without intervention, while others display aggressive behavior, often resulting in death due to recurrent or refractory metastatic disease despite multimodal therapy [5]. The Children's Oncology Group (COG) NB risk classification system categorizes patients into low-, intermediate-, and high-risk groups [6]. Non-high-risk patients have an overall survival (OS) rate exceeding 90%, yet high-risk patients have long-term survival rates below 50% even after intensive multidisciplinary treatment [7]. Therefore, elucidating the heterogeneity of neuroblastoma, identifying new prognostic markers, and developing innovative treatment strategies are of paramount importance in improving the survival rates of NB patients.

Tumor metabolic reprogramming is a hallmark in cancer cells. Fatty acid metabolism plays an important role in sustaining normal physiological functions in the human body, serving as a source of energy, providing substrates for cell membrane synthesis, and supplying precursors for bioactive molecules. Cancer cells are especially reliant on lipid metabolism for energy generation, as lipids are fundamental constituents of cellular membranes and reservoirs of precursors for biologically active lipid mediators [8, 9]. Therefore, fatty acid metabolism may play an important role in NB. Studies have shown that MYCN can upregulate FATP27, the fatty acid transport protein encoded by SLC2A2, thereby promoting tumor proliferation [10]. However, other reports suggest that a diet rich in omega-3 (ω -3) polyunsaturated fatty acids (PUFAs) can inhibit growth of xenografted tumor cells [11]. Consequently, the role of fatty acid metabolism in neuroblastoma appears to be Janus-faced, with both promoting and inhibiting effects. Nonetheless, to date, no studies have systematically analyzed the impact of fatty acid metabolism in the context of neuroblastoma.

Fatty acid metabolism is also intimately connected to the tumor microenvironment. Accumulation of long-chain fatty acids within CD8+T cells leads to mitochondrial dysfunction and triggers transcriptional reprogramming of pathways involved in lipid metabolism, consequently reducing fatty acid catabolism. Specifically, CD8+T cells demonstrate down-regulation of the very-long-chain acyl-CoA dehydrogenase (VLCAD) enzyme, which exacerbates the buildup of long-chain fatty acids (LCFAs) and very-long-chain fatty acids (VLCFAs), contributing to lipotoxicity [12].

In this study, we developed a risk signature based on fatty acid metabolism genes (FMGs) and investigated the impact of the FMG-related risk signature on patient OS and the immune landscape. Additionally, we predicted the immunotherapy and chemotherapy responses for both the high-risk and low-risk group. Our findings provide a precise and effective prognostic marker for neuroblastoma and may contribute to guiding treatment strategies for this disease.

2 Methods

2.1 Data acquisition and preprocessing

In this study, the workflow is illustrated in Figure S1A. Expression profile data and clinical pathological information of patients were retrieved separately from the Gene Expression Omnibus (GEO) dataset GSE49710 and the ArrayExpress dataset E-MTAB-8248. Expression profile data and clinical pathological information for neuroblastoma patients in the Therapeutically Applicable Research to Generate Effective Treatments (TARGET) program were obtained via the UCSC Xena database (<http://xena.ucsc.edu/>). After acquiring the RNA-seq data, samples without clinical pathological information were excluded from the three datasets. Subsequently, the probe IDs or Ensembl IDs were converted to gene symbols. The file detailing the correspondence between probe IDs and gene symbols for the GSE49710 and E-MTAB-8248 datasets is shown in Table S1. The file illustrating the correspondence between Ensembl IDs and gene symbols for the TARGET dataset is shown in Table S2. Rows or columns with more than 50% missing values in the expression profiles were removed. For genes with multiple entries, the median expression value was used. To standardize the data, $\text{Log}_2(\text{FPKM} + 1)$ transformation was applied to the expression profile data from the TARGET dataset. The expression profile data from GSE49710, E-MTAB-8248, and TARGET were batch-effect corrected using the “COMBAT” R package [13] (Fig. S1B-E). The

final GSE49710 dataset comprised 498 samples, which served as the training set. The E-MTAB-8248 dataset contained 223 samples, while the TARGET dataset included 151 samples; both E-MTAB-8248 and TARGET datasets were used as test sets. Baseline information for all samples is shown in Fig. S1F. A total of 308 fatty acid metabolism genes (FMGs) were sourced from a previous study [14]. The intersection of these FMGs with the RNA-seq data from GSE49710, E-MTAB-8248, and TARGET datasets resulted in 291 FMG-related genes that were used for further analysis.

2.2 Molecular subtype based on FMGs

We applied consensus clustering using the R package “ConsensusClusterPlus” to the GSE49710 dataset, to determine the molecular subtype based on FMGs [15]. The number of clusters k was incrementally varied from 2 to 9, and the optimal value was determined by assessing the delta area, cumulative distribution function (CDF), and consensus matrix. We used the Spearman correlation coefficient as the distance measure and performed 1000 iterations to ensure clustering stability. Principal component analysis (PCA) was then employed to evaluate the clustering effect. Kaplan–Meier (K–M) survival curves were generated using the “survival” R package to assess OS in patients across different subtypes [16]. Finally, we compared the distribution of clinical-pathological features and FMGs expression between patients in distinct subtypes.

2.3 Screening FMGs associated with patient prognosis

Using the “survival” R package [17], we performed univariate Cox regression analysis on the 291 FMGs in conjunction with the clinical survival outcome information from the GSE49710 dataset. For binary variables, we assigned a value of 0 to favorable factors and 1 to adverse factors. For multicategorical variables, we introduced dummy variables for analysis. This analysis aimed to identify FMGs significantly associated with OS. A p -value threshold of <0.05 was considered statistically significant.

2.4 Construction and validation of the FMG-related risk signature

The FMGs significantly associated with OS were used to establish an FMG-related risk signature. For the GSE49710 dataset, comprising 498 samples, we further refined the gene selection using LASSO analysis with the “glmnet” package [18]. We employed tenfold cross-validation to estimate the confidence intervals for each lambda value and determined the optimal lambda with the lowest mean error. Subsequently, we performed backward stepwise multivariate Cox regression to reduce the number of genes and obtain regression coefficients for each gene. Finally, coefficients for the selected gene combination based on the LASSO-Cox regression and their expression levels in the samples of GSE49710 dataset, we constructed the FMG-related risk signature, with the risk score calculated as follows:

$$\text{Riskscore} = \sum \text{Exp}(i) \times \text{Coef}(i)$$

where $\text{Coef}(i)$ is the coefficient of each FMG and $\text{Exp}(i)$ is the expression level of each FMG. In the E-MTAB-8248 and TARGET datasets, the risk score for each patient was calculated using the same coefficients and standardized RNA-seq profile data for the FMGs. Afterwards, samples in GSE49710 dataset were divided into two groups based on the median risk score. Samples above the median risk score were considered the high-risk group, while those below were deemed the low-risk group. Based on the median risk score from the GSE49710 dataset, the samples from the E-MTAB-8248 and TARGET datasets were divided into two groups. Samples with a risk score higher than the median risk score from the GSE49710 dataset were classified as the high-risk group, while those with a risk score lower than the median were classified as the low-risk group. Survival analysis for OS probability was conducted using the “survival” R packages to evaluate the prognostic value of the risk signature. Receiver Operating Characteristic (ROC) curve analysis was performed using the “pROC” R package [19] to assess the specificity and sensitivity of the risk signature. Principal Component Analysis (PCA) was utilized to verify if it could distinguish between different clusters obtained from different risk groups based on the FMG-related risk signature. Following this, we utilized the “rms” R package to plot C-index curves [20], which allowed us to compare the predictive ability of the FMG-related risk signature with clinical features in the dataset for OS. Finally, we examined the distribution of clinical features across different risk groups and explored the relationship between risk scores and clinical features to evaluate their potential for clinical application.

For decision curve analysis (DCA), we amalgamated clinical information from three datasets to augment statistical power, retaining categorical variables in their original non-numeric form. Through stratification of the patient population into relevant subgroups defined by age at diagnosis, MYCN status, and INSS stage, we performed Cox proportional hazards models to calculate the risk probabilities of the FMG-related risk score or categorical variables at the median time of death events. Finally, we performed DCA using the “dcurves” R package and plotted the DCA curves.

2.5 Prognostic analysis and construction of a nomogram

Using the “survival” R package, we performed univariate and multivariate Cox regression analyses on the FMG-related risk signature and established clinical prognostic indicators for three datasets to determine the predictive value of the FMG-related risk signature in the context of these established clinical indicators. The handling of variables was conducted as previously described. Subsequently, we used the FMG-related risk signature and the established clinical prognostic indicators that were common to all three datasets to construct a nomogram in the next step. Additionally, considering the potential impact of MYCN on fatty acid metabolism, to avoid incorporating MYCN's influence redundantly and to further simplify the nomogram, we included only age, international neuroblastoma staging system (INSS) stage, and FMG-related risk group in constructing the nomogram. To enhance clinical applicability in nomogram implementation, the continuous variable of patient age was dichotomized into < 2 years and > 2 years. Furthermore, employing the “rms” R package, we constructed a nomogram to predict OS probabilities at 1, 5, and 10-year intervals. Calibration curves were generated to evaluate the precision of the nomogram predictions.

2.6 Single-sample gene set enrichment analysis (ssGSEA)

In this study, we calculated the enrichment scores for multiple gene sets in each sample of the GSE49710 dataset using the ssGSEA algorithm from the “GSVA” R package [21]. These gene sets primarily included those related to the antigen processing and presenting machinery (APM), the MHC-I protein complex pathway, 30 distinct types of tumor microenvironment (TME) cells, 13 gene sets associated with immune functions, and a gene set related to NK cell cytotoxicity.

2.7 Immune landscape of the risk signature

The antigen processing and presenting machinery (APM) score (APMS), derived through ssGSEA of 18 genes associated with APM, serves as an indicator of antigen processing and presentation efficiency [22]. We acquired the gene set for the MHC-I protein complex pathway from the MSigDB (<https://www.gsea-msigdb.org/gsea/msigdb>) and performed ssGSEA. The enrichment scores calculated were indicative of MHC-I activity. In the analysis of the immune infiltration landscape, ssGSEA was employed to quantify the enrichment scores of 30 distinct types of tumor microenvironment (TME) cells (Table S3). The “ESTIMATE” algorithm [23] was used to compute immune, stromal, and ESTIMATE scores, providing insights into the immune microenvironment across different groups. For the assessment of immune function, we obtained 13 gene sets related to various immune functions (Table S4) and a gene set for natural killer (NK) cell cytotoxicity from the Immunology Database and Analysis Portal (ImmPort) (Table S5). Using the ssGSEA algorithm, we evaluated the immune function and NK cell cytotoxicity of different risk groups. To compare the differences in the immune landscape between different FMG-related risk groups, we used the Wilcoxon test to determine if there were statistically significant differences in the enrichment scores for the various gene sets among the different risk groups. Additionally, we calculated the Spearman correlation coefficients to assess the relationships between APMS, MHC-I activity, infiltration level of activated CD8+ T cells, infiltration level of NK cells, NK cell cytotoxicity, and the risk score. We also extracted the encoding genes for NK cell-activating receptors and their ligands and compared their expression levels between different risk groups to evaluate NK cell activation. A *p*-value threshold of < 0.05 was considered statistically significant.

2.8 Prediction of chemotherapy response

The chemotherapy sensitivity of the high-risk group and the low-risk group was characterized by predicting the half-maximal inhibitory concentration (IC50) of chemotherapeutic drugs using the R package “oncoPredict” [24]. The Wilcoxon

test was used to check for statistically significant differences in the IC50 values of each chemotherapy drug between the different risk groups. A p -value threshold of < 0.05 was considered statistically significant.

2.9 Expression of immune checkpoint genes in FMG-related risk groups

The responsiveness to immunotherapy is often linked to the expression levels of immune checkpoint genes. We extracted the expression levels of 46 immune checkpoint genes from the GSE49710 dataset [25], including *ADORA2A*, *BTLA*, *BTNL2*, *CD160*, *CD200*, *CD200R1*, *CD244*, *CD27*, *CD274*, *CD276*, *CD28*, *CD40*, *CD40LG*, *CD44*, *CD48*, *CD70*, *CD80*, *CD86*, *CTLA4*, *HAVCR2*, *HLA2*, *ICOS*, *ICOSLG*, *IDO1*, *IDO2*, *KIR3DL1*, *LAG3*, *LAIR1*, *LGALS9*, *NRP1*, *PDCD1*, *PDCD1LG2*, *TIGIT*, *TMIGD2*, *TNFRSF14*, *TNFRSF18*, *TNFRSF25*, *TNFRSF4*, *TNFRSF8*, *TNFRSF9*, *TNFSF14*, *TNFSF15*, *TNFSF18*, *TNFSF4*, *TNFSF9*, *VTCN1*. We compared the expression levels of these genes across different FMG-related risk groups to determine if there were any significant differences. A p -value threshold of < 0.05 was considered statistically significant.

2.10 Hallmark gene sets enrichment analysis of FMG-related risk group

We obtained hallmark gene sets from the MSigDB database. Through the “GSVA” R package, we conducted ssGSEA on different risk groups, and respectively visualized the data in the heatmap.

2.11 Identification of differential expressed genes between groups and functional enrichment analysis

To conduct differential expression analysis between two risk groups, the “limma” R package was utilized [26]. Genes meeting the criteria of $|\log_2 \text{Fold Change}| \geq 1.5$ and adjusted p -value < 0.05 were classified as differentially expressed genes (DEGs). Further, functional enrichment analysis of these DEGs was performed using the “clusterProfiler” R package [27], encompassing analysis of Gene Ontology (GO) and Kyoto Encyclopedia of Genes and Genomes (KEGG) pathways.

2.12 Construction of protein–protein interaction (PPI) networks and identification of hub genes

The genes comprising the 35 genes in risk signature were uploaded to the STRING database (version 12.0) to elucidate their interactive networks [28]. The protein–protein interaction (PPI) score was set at 0.40. The resultant network was then imported within Cytoscape (version 3.10.2). Following this, the cytoHubba plugin was employed to screen for the top 10 hub genes, with the screening methodology anchored on the Maximal Clique Centrality (MCC) scoring system.

3 Results

3.1 Identification of two subtypes of neuroblastoma based on FMGs

To investigate the association between FMGs and NB, we performed consensus clustering on the 498 samples in the GSE49710 dataset. Based on the changes in the relative CDF and delta area, the CDF curve showed the flattest middle part and the consensus matrix had the clearest boundaries when $k = 2$ (the number of clusters) (Fig. S1G–H). Therefore, we divided the samples in the GSE49710 dataset into two clusters, designated as Cluster 1 and Cluster 2 (Fig. 1a). The results of PCA demonstrated that the most patients in these two clusters could be differentiated (Fig. 1b). Furthermore, a prognosis analysis conducted on the two clusters revealed that patients in cluster 2 had significantly worse prognoses ($p < 0.0001$) (Fig. 1c). There were also noticeable differences in the distribution of clinical and pathological information between the two clusters. For instance, cluster 2 contained a higher number of patients with high clinical risk, *MYCN* amplification, and INSS stage 4, compared to cluster 1 (Fig. 1d).

3.2 Construction and validation of FMG-related risk signature

To investigate the impact of FMGs on patient prognosis and establish a corresponding risk signature, we conducted univariate Cox regression analysis, ultimately narrowing down to 207 genes for further analysis (Table S6). Regression coefficients for each gene were estimated using LASSO-Cox regression, and the optimal lambda ($\lambda = 0.0236410595011078$)

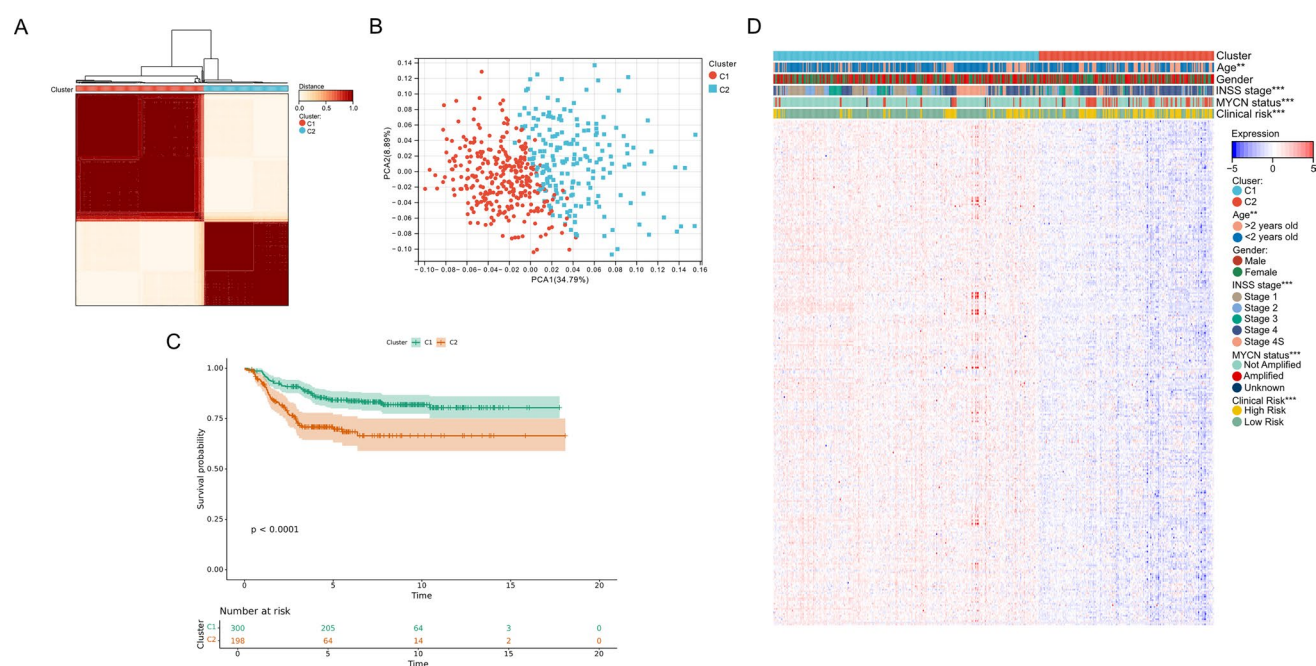


Fig. 1 Identification of FMG-related clusters in the training set. **a** Identification of two FMG-related clusters according to the consensus clustering matrix ($k=2$) in the GSE49710 cohort. **b** PCA result of two clusters. **c** Kaplan–Meier curves of OS in the GSE49710 cohort between different clusters. **d** Comparison of clinical characteristics and expression profiles of FMGs in different clusters within the GSE49710 cohort

was determined through ten-fold cross-validation (Fig. 2a, b). The formula for calculating the risk score for each patient is shown in Table S7.

Patients from three datasets were segregated into two groups based on the median risk score of 4.881317279 derived from the GSE49710 dataset; those above this threshold were classified as high-risk group, while those below were designated low-risk group. In the GSE49710 dataset, an escalation in risk score corresponded with a rising mortality risk among patients (Fig. 2c). The expression levels of 35 FMGs showed a discernible correlation with increasing risk scores. For instance, genes such as *ABCC1*, *CBR1*, *CPT1C*, *ELOVL6*, and *ODC1* exhibited heightened expression alongside rising risk scores, whereas *ACADVL*, *AKR1C3*, *CROT*, *GPD1*, and *GPD2* displayed decreasing expression levels as risk scores climbed (Fig. 2c). The PCA outcomes illustrated that the two patient groups were largely distinguishable (Fig. 2d), and survival rates were notably lower for the high-risk group than for the low-risk group ($p < 0.0001$) (Fig. 2e). The ROC curve yielded area under curve (AUC) values of 0.93, 0.94, and 0.95 at 1-year, 3-year, and 5-year intervals, respectively (Fig. 2f). Subsequent computations of C-indexes for the FMG-related risk signature and several clinical parameters revealed the FMG-related risk signature boasted the highest C-index (Fig. 2g), indicative of superior predictive power.

We applied the same risk signature formula to calculate risk scores for E-MTAB-8248 and TARGET datasets, to validate the FMG-related risk signature. Consistent with the GSE49710 dataset findings, both E-MTAB-8248 (Fig. 3a–e) and TARGET (Fig. 3f–j) datasets, mirrored similar trends. An increase in risk score paralleled greater mortality risk in the patients, with the expression levels of the 35 genes maintaining a relevant association with risk scores (Fig. 3a, f). PCA was able to distinguish most of the patients into two groups (Fig. 3b, g). In the E-MTAB-8248 dataset, AUCs were 0.75, 0.76, and 0.88 at 1, 3, and 5 years, respectively (Fig. 3c). For the TARGET dataset, AUCs at 1, 3, and 5 years were 0.61, 0.68, and 0.67, respectively (Fig. 3h). Kaplan–Meier (K–M) analysis underscored poorer prognoses for the high-risk group ($p < 0.05$) (Fig. 3d, i). The FMG-related risk model maintained the highest C-index across both E-MTAB-8248 and TARGET datasets (Fig. 3e, j), further substantiating its predictive capacity. Additionally, considering the potential association between *MYCN* and FMGs, and the fact that *MYCN* amplification may influence many downstream signaling pathways, we investigated whether *MYCN* amplification status affects the performance of the FMG-related risk signature. To validate this, we combined the patients from the three datasets and divided them into two groups: those with *MYCN* amplification and those without. We then calculated the C-index for the FMG-related risk signature, age, and INSS stage in both groups. The results indicated that the FMG-related risk signature had the highest C-index (Fig. S2).

To assess the clinical value of the FMG-related risk signature, we performed decision curve analysis (DCA) comparing its net benefit against existing factors (age, *MYCN* status, INSS stage, and clinical risk). Results showed the FMG-related

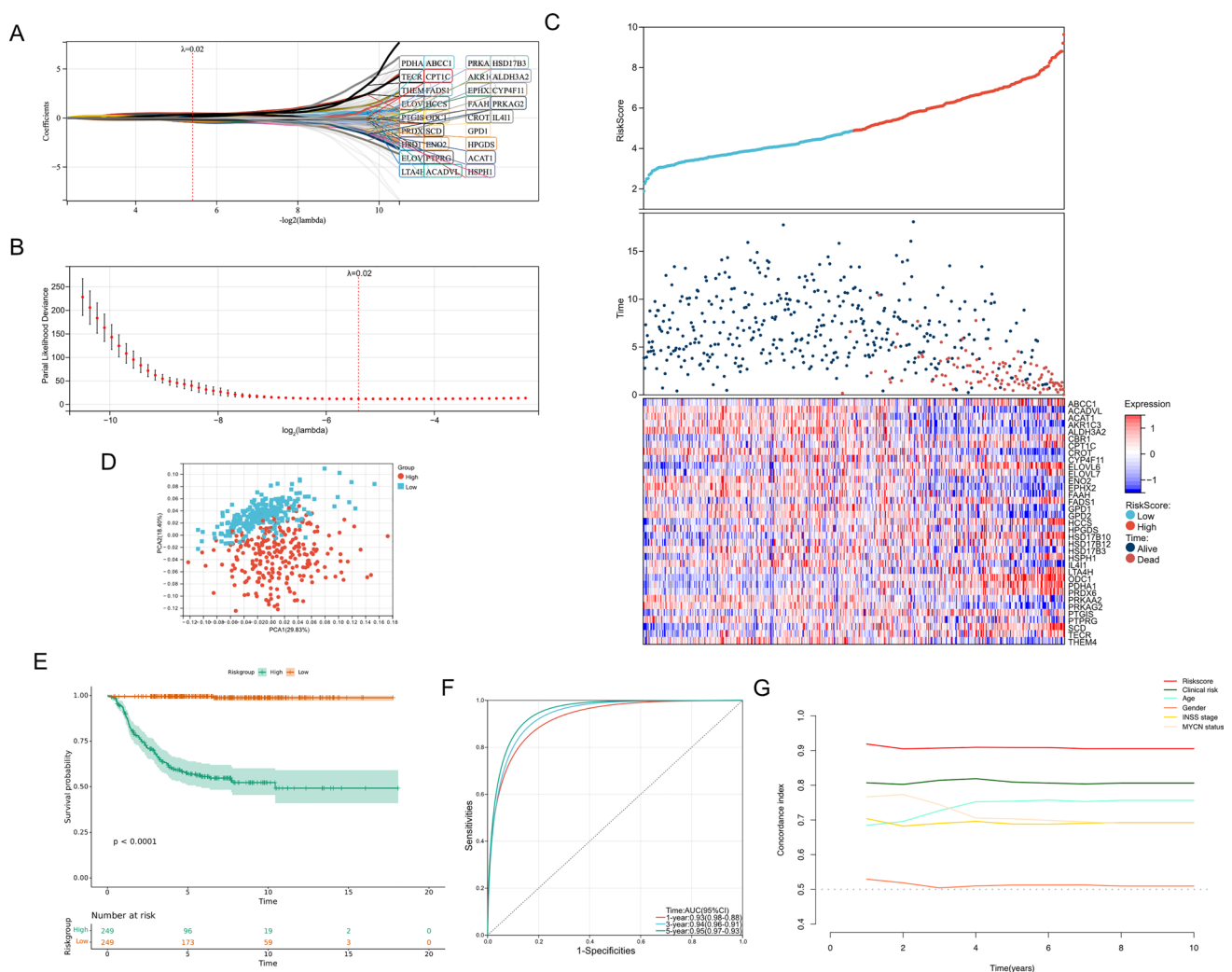


Fig. 2 Development of FMG-related risk signature in the training set. **a, b** The LASSO-Cox regression analysis was performed depending on the optimal λ value. **c** The distributions of OS status and patient survival status, and RNA profiles of 35 FMGs in risk signature in the GSE49710 cohort. **d** PCA was able to distinguish most of the samples. **e** The Kaplan–Meier curves showed that significant differences were identified for OS between the two risk groups. **f** ROC curves evaluating the sensitivity and specificity of the FMG-related risk signature. **g** C-index of the risk signature and other clinical characteristics

risk signature provided higher net benefit across wider probability thresholds than other variables in all patients (Fig. 4a). We further validated its performance in subgroups divided by age, MYCN status, and INSS stage. The FMG-related risk signature maintained superior net benefit in all subgroups, covering broader threshold ranges than traditional clinical risk criteria (Fig. 4b–l). These findings confirm the FMG-related risk signature’s clinical utility for personalized decision-making.

3.3 The correlation between FMG-related risk signature and clinical characteristics

Within the GSE49710 dataset, we corroborated the associations between patient clinical characteristics and risk scores, revealing significant correlations between risk scores and MYCN status, INSS stage, age, and clinical risk (Fig. 5a). Specifically, higher risk scores were markedly associated with patients older than 2 years, amplified MYCN status, advanced INSS stages, and high clinical risk (Fig. 5b–e). We then investigated the impact of risk scores on survival within various patient subgroups, finding that individuals in the high-risk group consistently experienced shorter survival times compared to those in the low-risk group across different subgroups (Fig. 5f–m). Similar results could be found in the E-MTAB-8248 (Fig. S3) and TARGET datasets (Fig. S4).

To ascertain the predictive value of the FMG-related risk signature in the context of these established clinical indicators, we conducted univariate and multivariate Cox regression analyses in three datasets. Results demonstrated that risk scores

Fig. 3 Validation of FMG-related risk signature in the testing sets. The distributions of OS status and patient survival status, and RNA profiles of 35 FMGs in risk signature in the E-MTAB-8248 (a) and TARGET cohorts (f). PCA was able to distinguish most of the samples in the E-MTAB-8248 (b) and TARGET cohorts (g). ROC curves evaluating the sensitivity and specificity of the FMG-related risk signature in the E-MTAB-8248 (c) and TARGET cohorts (h). The Kaplan–Meier curves showed that significant differences were identified for OS between the two risk groups in the E-MTAB-8248 (d) and TARGET cohorts (i). C-index of the risk signature and other clinicopathological characteristics in the E-MTAB-8248 (e) and TARGET cohorts (j)

were significantly associated with OS in patients, thereby qualifying as an independent prognostic factor in the GSE49710 (Fig. 6a, b), E-MTAB-8248 (Fig. S5A, B) and TARGET (Fig. S5D, E) datasets. Seeking to enhance the clinical applicability for personalized prognosis predictions, we integrated risk scores with multiple clinical risk factors in the GSE49710 dataset to construct a nomogram (Fig. 6c). This nomogram assigned a score to each prognostic factor, allowing for the prediction of 1-year, 5-year, and 10-year OS based on the cumulative scores for each sample (Fig. 6c). To evaluate the accuracy of the nomogram, calibration curves were utilized, demonstrating close agreement between predicted and actual survival probabilities at 1, 3, 5, and 10 years (Fig. 6d). Consistent results were also observed in the E-MTAB-8248 (Fig. S5C) and TARGET (Fig. S5F) datasets. Additionally, after integrating the patients from the three datasets and further classifying them, we found that in most classifications, the high-risk group had significantly worse OS compared to the low-risk group (Fig. S6).

3.4 Immune landscape of NB based on FMG-related risk signature

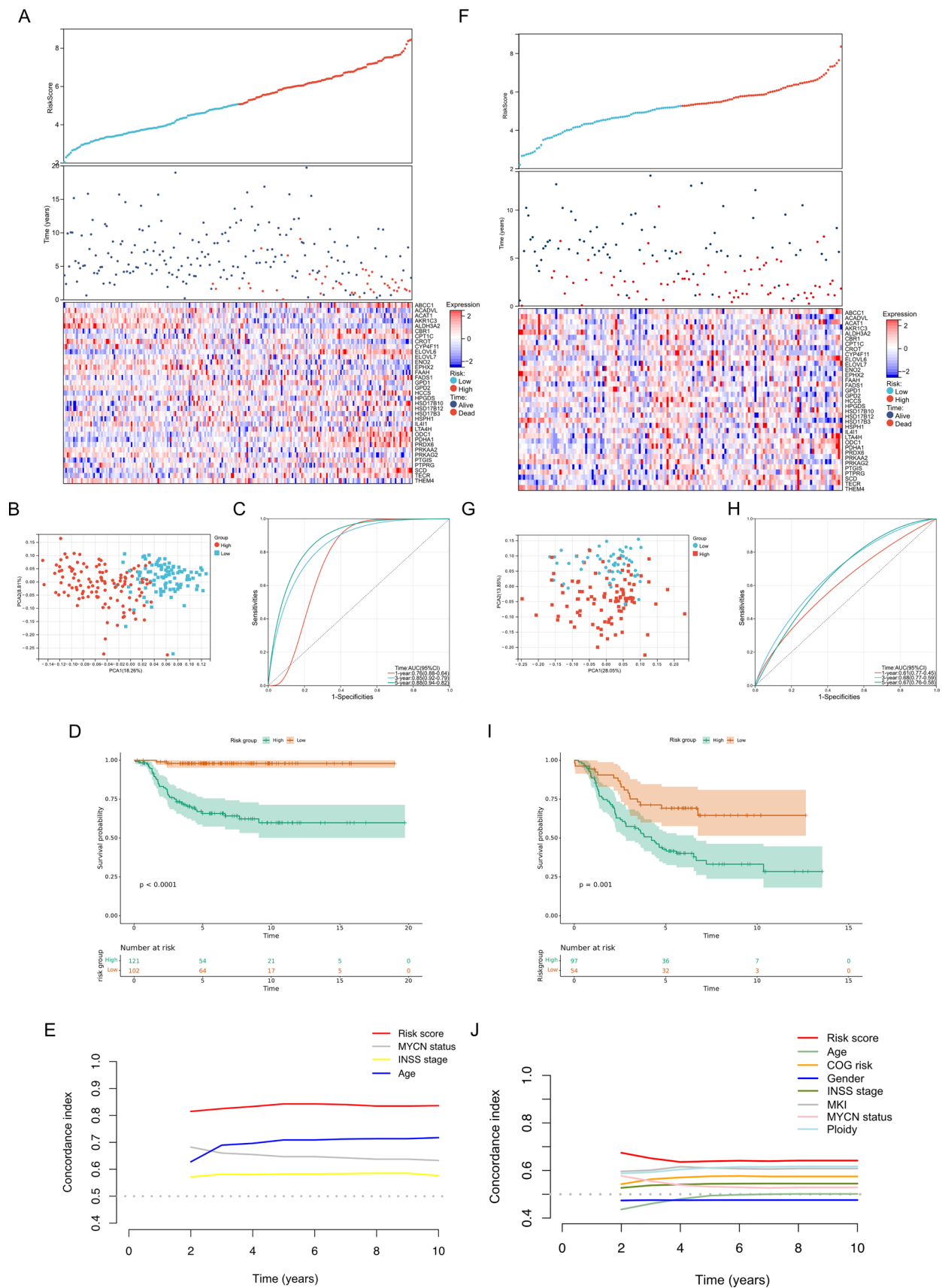
It has been reported that impairment of the antigen-presenting machinery (APM) is a critical contributor to the low immunogenicity of neuroblastoma [29]. To assess antigen presentation capabilities in patients, we employed an antigen presenting machine score (APMS), which revealed that patients in the high-risk group had significantly lower APMS compared to those in the low-risk group, with APMS showing a strong negative correlation with risk scores (Fig. 7a). Given the pivotal role of MHC class I molecules in antigen presentation, we utilized an MHC score to evaluate MHC-I activity. Our findings indicated that patients in the high-risk group had significantly lower MHC scores than those in the low-risk group, with MHC scores exhibiting a pronounced negative correlation with risk scores (Fig. 7b). Diminished antigen presentation often impedes the recognition of tumor cells by CD8+T cells, leading to immune evasion—a phenomenon consistent with our observation of a positive correlation between MHC-I activity and activated CD8+T cell infiltration (Fig. S7), coupled with a significant negative correlation between risk scores and activated CD8+T cell infiltration (Fig. 7c). These results suggest that antigen presentation is considerably weakened in the high-risk group relative to the low-risk group, with decreased MHC-I activity potentially underlying the reduced infiltration of activated CD8+T cells.

To comprehensively evaluate the infiltration of immune and stromal cells in patients across different risk groups, we calculated ESTIMATE scores. Patients in the high-risk group had significantly lower immune and stromal scores than those in the low-risk group (Fig. 7d). Moreover, the low-risk group featured not only higher infiltration levels of most immune cells (Fig. 7e) but also higher scores for various immune functions (Fig. 7f), indicating that mechanisms of immune evasion result in reduced infiltration and functionality of multiple immune cell types in the high-risk group.

Natural Killer (NK) cells, known for their potential to kill tumors, are markers of favorable prognosis, with active NK cells associated with better outcomes in neuroblastoma patients [30]. Upon evaluating NK cell infiltration and NK cell activity, we found that patients in the high-risk group had lower levels of NK cell infiltration and NK cell activity compared to those in the low-risk group, with both NK cell infiltration and activity showing a significant negative correlation with risk scores (Fig. 7g, h). These findings suggest that reduced NK cell activity is another consequence of immune evasion in the high-risk group.

Recognizing the immense potential of immunotherapy, we assessed the expression levels of immune checkpoint genes in patients across different risk groups. Among 46 immune checkpoint genes, 41 displayed higher expression levels in the low-risk group than in the high-risk group (Fig. 7i), suggesting the relevance of immune checkpoint genes expression patterns to risk stratification and potential therapeutic targets.

Additionally, *MYCN* amplification is a characteristic genetic alteration in NB and, as a member of the *MYC* family, has significant implications. For patients without *MYCN* amplification, we observed that compared to the low-risk group, the high-risk group had lower MHC scores (Fig. S8A), lower NK cell infiltration (Fig. S8B), and lower NK cell activity (Fig. S8C). Additionally, the levels of multiple immune cell infiltrations were also changed in the high-risk group (Fig. S8D). However, there was no difference in APMS (Fig. S8E) or activated CD8+T cell infiltration levels (Fig. S8F) between the two groups. In terms of immune checkpoint gene expression, 34 immune checkpoint genes showed differential expression



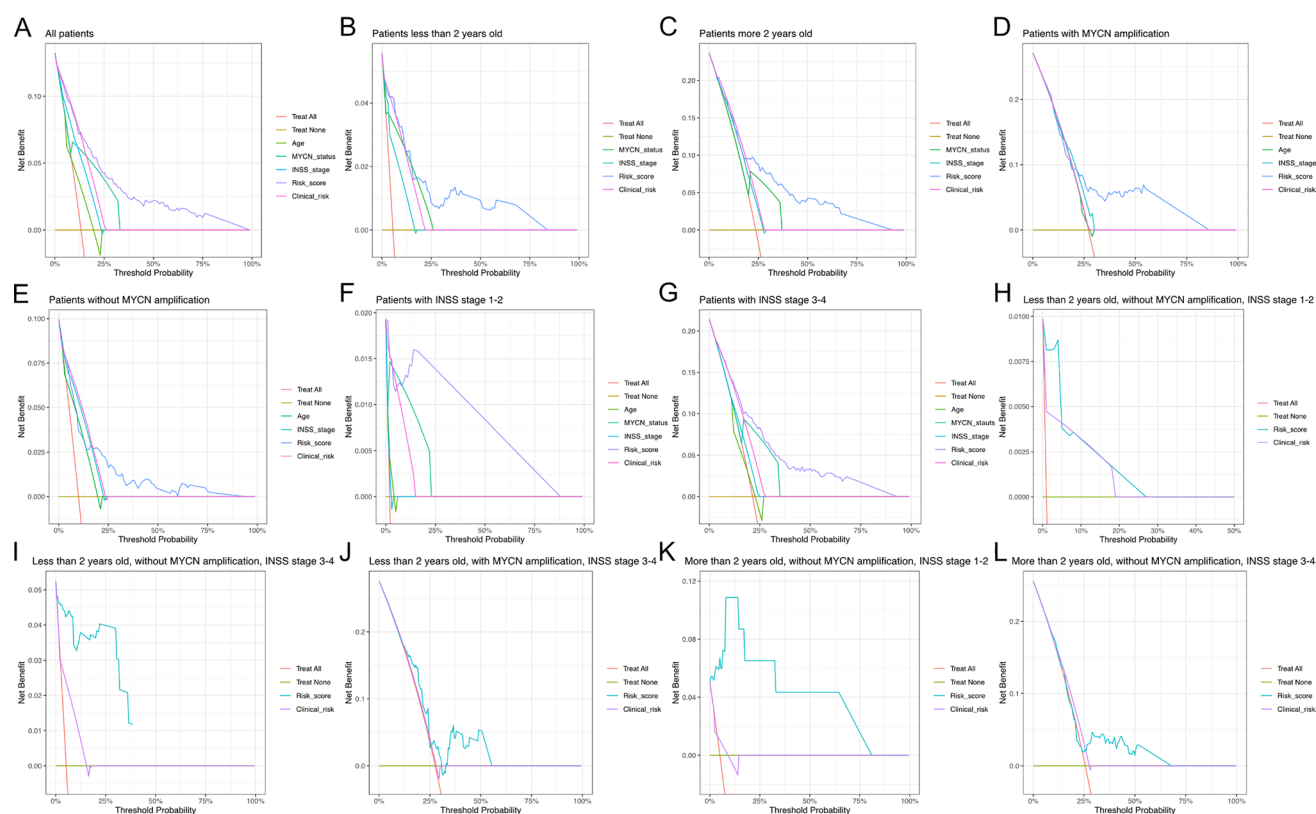


Fig. 4 DCA curves across patient subgroups. **a** DCA curve for all patients. **b** Patients aged < 2 years. **c** Patients aged > 2 years. **d** Patients with MYCN amplification. **e** Patients without MYCN amplification. **f** INSS stage 1–2 patients. **g** INSS stage 3–4 patients. **h** Patients aged < 2 years without MYCN amplification and INSS stage 1–2 disease. **i** Patients aged < 2 years without MYCN amplification and INSS stage 3–4 disease. **j** Patients aged < 2 years with MYCN amplification and INSS stage 3–4 disease. **k** Patients aged > 2 years without MYCN amplification and INSS stage 1–2 disease. **l** Patients aged > 2 years with MYCN amplification and INSS stage 3–4 disease

between the high-risk and low-risk groups in patients without *MYCN* amplification (Fig. S8G). These results suggest that *MYCN* may play a crucial role in the immune microenvironment.

In summary, these comprehensive analyses reveal the intricate interplay between risk scores, antigen presentation, immune cell infiltration, and NK cell activity, highlighting the critical role of immune evasion in the pathogenesis and prognosis of neuroblastoma.

3.5 Functional enrichment analysis and screening the hub genes of FMG-related risk signature

The comparative analysis of potential biological alterations between two risk groups was conducted using ssGSEA, Kyoto Encyclopedia of Genes and Genomes (KEGG) pathway analysis, and Gene Ontology (GO) enrichment analysis. The ssGSEA results revealed that pathways related to DNA repair, cell cycle regulation, and cellular metabolism were significantly enriched in the high-risk group, including DNA_REPAIR, MITOTIC_SPINDLE, G2M_CHECKPOINT, OXIDATIVE_PHOSPHORYLATION, MTORC1_SIGNALING, and GLYCOLYSIS. In contrast, the low-risk group showed significant enrichment in signaling pathways and tumor suppressor pathways such as HEDGEHOG_SIGNALING, TGF_BETA_SIGNALING, WNT_BETA_CATENIN_SIGNALING, IL2_STAT5_SIGNALING, and IL6_JAK_STAT3_SIGNALING (Fig. 8a).

Subsequently, KEGG pathway enrichment and GO enrichment analyses were performed on differentially expressed genes (DEGs) between the two groups. The KEGG results highlighted significant enrichment in pathways such as PI3K-Akt signaling pathway, cAMP signaling pathway, Phospholipase D signaling pathway, and TNF signaling pathway (Fig. 8b). Bubble plots were constructed for the top 10 enriched pathways within the three functional categories of GO analysis—Biological Process (BP), Cellular Component (CC), and Molecular Function (MF)—where BP pathways were mainly associated with cell adhesion, CC with membrane-bound structures, and MF with ion channel and receptor activities (Fig. 8c).

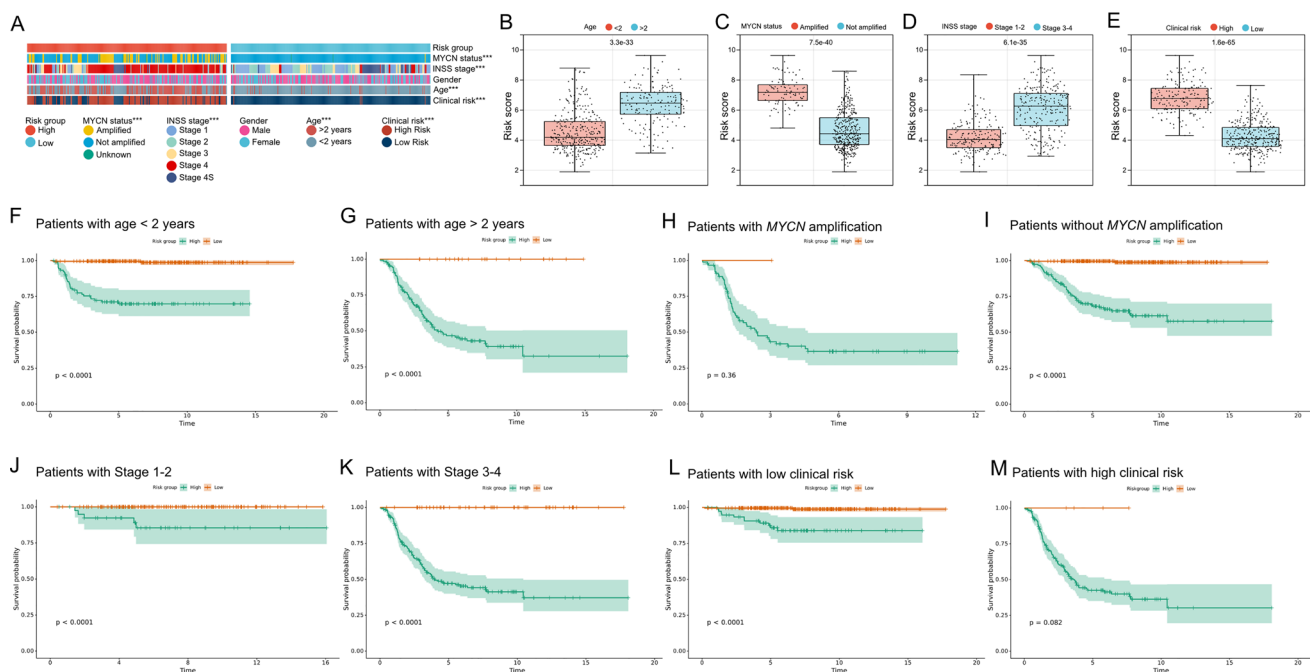


Fig. 5 Correlation analysis between clinical characteristics and the risk signature in training set. **a** Correlation analysis between the risk signature and clinical characteristics in GSE49710 cohort. **b–e** The comparison of risk scores between samples with different clinical characteristics, including INSS age (**b**), *MYCN* status (**c**), INSS stage (**d**), and clinical risk groups (**e**). **f–m** The prognostic role of the FMG-related risk signature was studied in different variable subgroups. (* $p < 0.05$, ** $p < 0.01$, *** $p < 0.001$)

Following this, an interaction network for proteins encoded by 35 FMG-related risk signature genes was plotted (Fig. 8d), and 10 hub genes were identified through screening in Cytoscape. These hub genes are *HSD17B12*, *SCD*, *FADS1*, *TECR*, *ELOVL6*, *ACADVL*, *CBR1*, *AKR1C3*, *HPGDS*, and *EPHX2* (Fig. 8e). These genes could play crucial roles in the disease's pathology or serve as potential targets for therapy.

3.6 Prediction of drug sensitivity

The significant differences observed across various parameters between the two risk groups prompted us to compare their drug sensitivities. Our findings indicated that compared to the low-risk group, patients in the high-risk group exhibited greater sensitivity to Tivozanib, Ulixertinib, Refametinib, and Sorafenib (Fig. 9a–d). Conversely, patients in the low-risk group showed higher sensitivity to Savolitinib, Axitinib, Lapatinib, and Erlotinib when compared to the high-risk group (Fig. 9e–h). The mechanisms of action for these drugs are summarized in Table S8.

4 Discussion

Neuroblastoma (NB) accounts for 15% of all childhood cancer-related deaths, characterized by its high heterogeneity, which leads to vastly differing patient outcomes and poses significant challenges to current therapeutic paradigms [31]. Therefore, identifying and establishing accurate and effective prognostic prediction models is essential for improving treatment efficacy. In this study, we identified two NB subtypes with distinct fatty acid metabolism patterns, underscoring the significance of FMGs in NB. Subsequently, we established a risk signature based on 35 FMGs through the LASSO-Cox method and validated its discriminatory power and accuracy across three datasets. Moreover, the FMG-related risk signature demonstrated substantial correlations with clinical prognostic features. We also developed and validated a nomogram integrating the FMG-related risk signature with several clinical prognostic factors. In summary, we have developed a novel FMG-related risk signature for NB, capable of achieving reliable and personalized prognostic predictions.

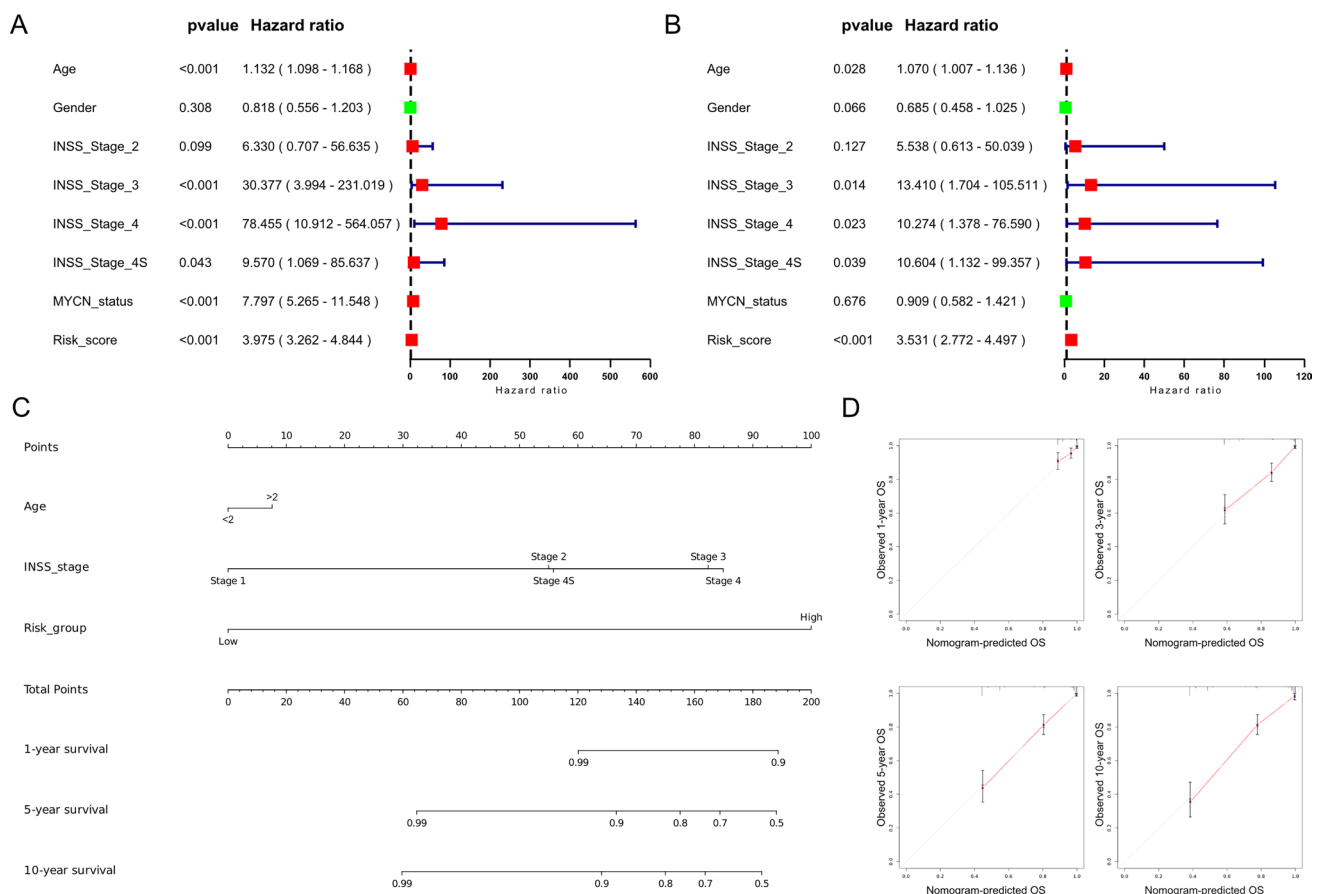


Fig. 6 Independent prognosis analysis of the risk signature and construction of a nomogram for 1-year, 5-year and 10-year OS prediction. **a** The univariate Cox regression analysis in GSE49710 cohort. **b** The multivariate Cox regression analysis in GSE49710 cohort. **c** The establishment of a nomogram that predicted 1-year, 5-year and 10-year in the GSE49710 cohort. **d** Calibration curves of the nomogram in the prediction of 1-year, 3-year, 5-year and 10-year OS in GSE49710 cohort

In the FMG-related risk signature comprising 35 genes, the roles of most genes, including hub genes, remain largely unexplored in NB. *HSD17B12* encodes a crucial 17β -hydroxysteroid dehydrogenase, catalyzing reactions in the extension of long-chain fatty acids [32]. Studies have reported that the *HSD17B12* rs11037575>T polymorphism is significantly associated with NB susceptibility [33]. *SCD* codes for an enzyme involved in fatty acid biosynthesis, playing a key role in regulating the expression of genes engaged in lipogenesis and modulating mitochondrial fatty acid oxidation [34]. *SCD* protects tumor cells from ferroptosis induced by oxidative stress and plays a critical role in tumor recurrence after treatment with tyrosine kinase inhibitors (TKIs) and chemotherapy [35, 36]. *FADS1* encodes a protein belonging to the unsaturated fatty acid desaturase family, catalyzing the conversion of dihomo- γ -linolenic acid to arachidonic acid [37]. Upregulation of *FADS1* leads to increased sensitivity to ferroptosis in gastric cancer cells, and its expression levels correlate with the methylation status of its DNA [38]. It has been reported that silencing *FADS1* inhibits proliferation, migration, and invasion in squamous cell carcinoma cells [37], suggesting differential sensitivities and demands for its metabolites among various tumors, resulting in dual oncogenic and tumor-suppressive functions of *FADS1*. *TECR* encodes a protein belonging to the steroid 5- α reductase family, participating in the elongation of long-chain fatty acids [39], but its role in tumor cells remains unclear. *ELOVL6* encodes a protein primarily involved in the elongation of long-chain fatty acids, acting as the rate-limiting enzyme in this reaction. It is reported to be upregulated in liver cancer and associated with the development of hepatocellular carcinoma related to non-alcoholic steatohepatitis [40]. *ACADVL* encodes a protein whose main function is to catalyze the first step in mitochondrial β -oxidation of fatty acids [41]. Inhibition of *ACADVL* leads to ATP depletion and induces death in acute myeloid leukemia cells [42]. *AKR1C3* codes for a member of the aldo/keto reductase superfamily, catalyzing NADH and NADPH-dependent reduction of ketosteroids to hydroxysteroids [43]. It protects NB cells from damage caused by toxic aldehydes [44]. *HPGDS* is a member of the sigma class glutathione-S-transferase family. This enzyme catalyzes the conversion of PGH2 to PGD2 [45]. High levels of *HPGDS* have been associated with favorable

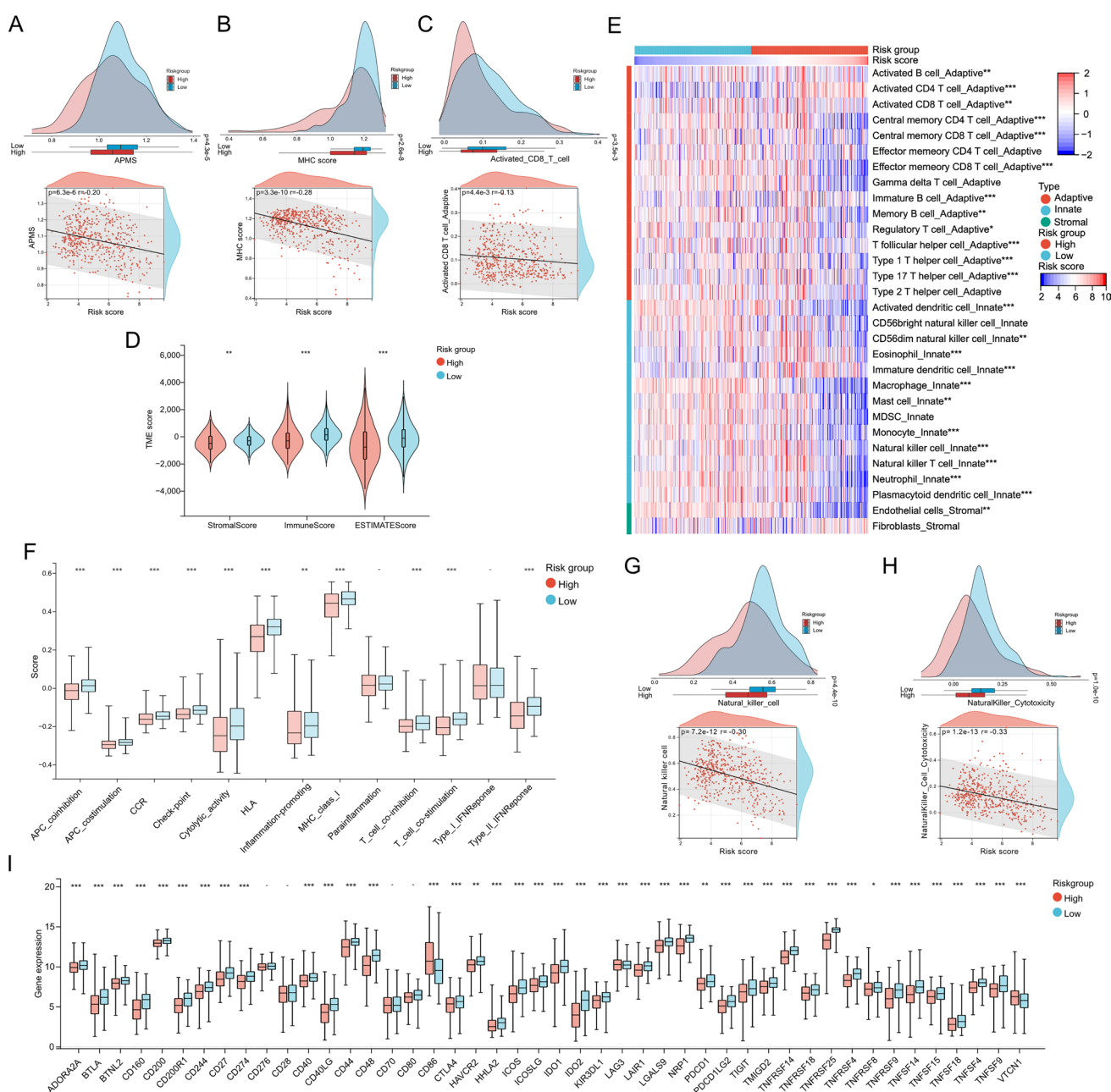


Fig. 7 The immune landscape of the risk signature. **a** The comparison of antigen-presenting machinery (APM) score between different risk groups (top) and correlation analysis between the risk score and the APM score (bottom). **b** The comparison of MHC score between different risk groups (top) and correlation analysis between the risk score and the MHC score (bottom). **c** The comparison of activated CD8+T cell infiltration between different risk groups (top) and correlation analysis between the risk score and the activated CD8+T cell infiltration (bottom). **d** The variance analysis of the ESTIMATE score, stromal score, and immune score in the different risk groups. **e** Different infiltration levels of immune infiltrating cells between low-risk and high-risk groups. **f** Analysis of immune functions in high-risk and low-risk groups. **g** The comparison of the NK cell infiltration level between different risk groups (top) and correlation analysis between the risk score and the NK cell infiltration level (bottom). **h** The comparison of the NK cell cytotoxicity between different risk groups (top) and correlation analysis between the risk score and the NK cell cytotoxicity (bottom). **i** The relationship between immune checkpoints and the FMG-related risk signature. (* $p < 0.05$, ** $p < 0.01$, *** $p < 0.001$)

outcomes in cancer patients [46, 47]. *CBR1* encodes a protein belonging to the short-chain dehydrogenase/reductase (SDR) family, an NADPH-dependent reductase with broad substrate specificity [48]. Reduced levels of *CBR1* decrease reactive oxygen species in pancreatic cancer cells, mitigating oxidative damage [49]. *EPHX2* encodes a member of the epoxide hydrolase family, a bifunctional enzyme with an epoxide hydrolase active site at the C-terminus [50] and a lipid

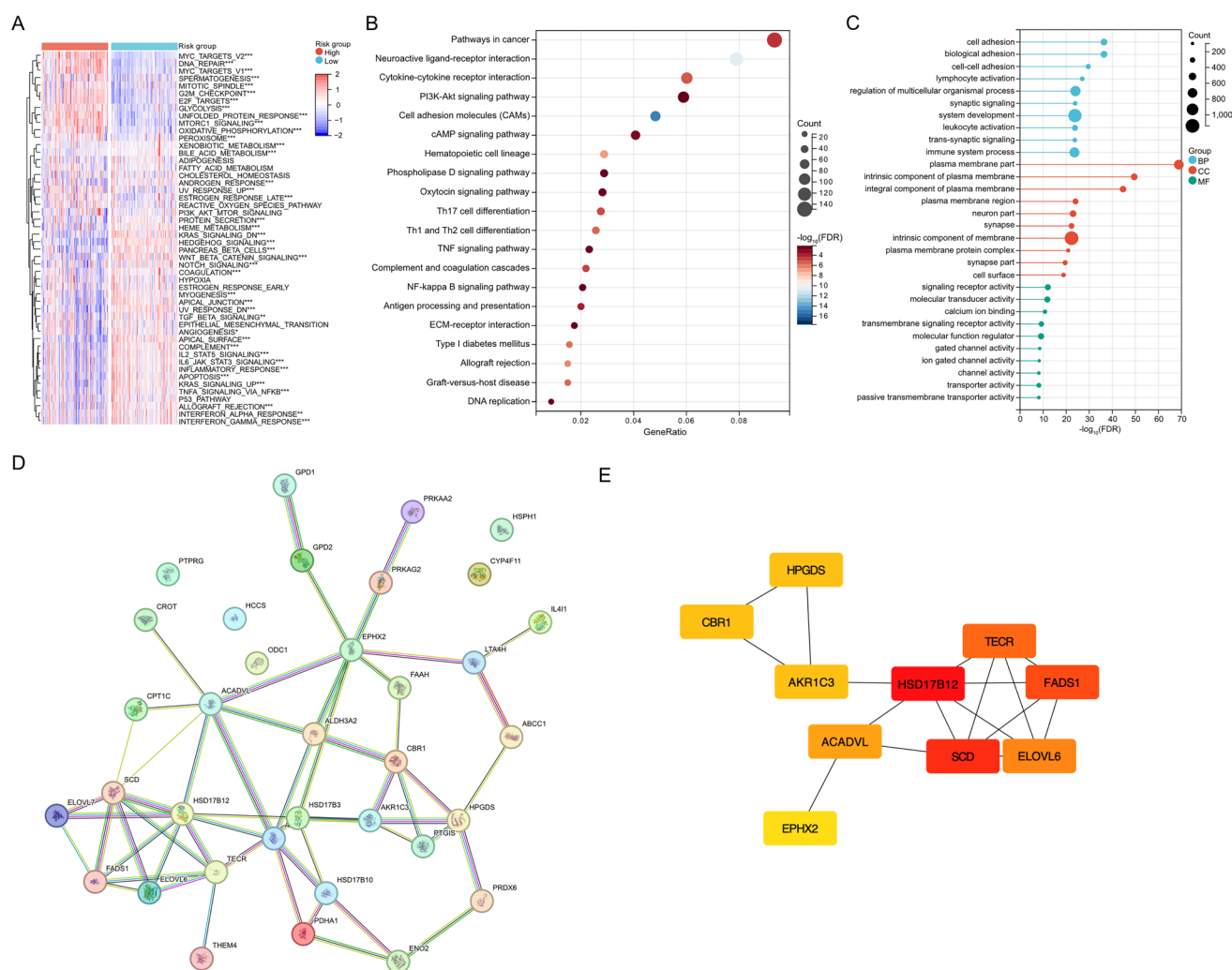


Fig. 8 Functional enrichment analysis and screening of hub genes. **a** The ssGSEA analysis of two risk groups in hallmark gene sets. **b** Functional annotation of DEGs by KEGG. **c** Functional annotation of DEGs by GO. **d** The PPI network of the 35 FMGs constructed with the STRING website. **e** The hub genes screened by Cytohubba

phosphatase activity at the N-terminus [51]. *EPHX2* is considered a tumor suppressor gene in multiple cancers [52–54], such as in prostate cancer where its mRNA and protein expression levels are significantly lower in tumors compared to normal prostate tissue, correlating negatively with Gleason grade and disease-free survival time [52]. In summary, these hub genes are intimately involved in fatty acid synthesis and metabolism, playing critical roles in tumorigenesis and tumor progression, thus supporting their predictive value for assessing the risk level in NB patients.

Neuroblastoma's low immunogenicity poses significant challenges to the development of immunotherapies, primarily due to reduced expression of MHC-I which triggers immune recognition. This results in difficulty for T cells and NK cells to identify tumor cells, leading to immune evasion [29, 55, 56]. Our findings suggest that the high-risk group exhibits lower APMS and diminished MHC-I activity, indicating reduced immunogenicity compared to the low-risk group. The high-risk group, characterized by low immunogenicity, shows a marked decrease in immune scores and reduced infiltration levels of various immune cells, especially CD8 + T cells and NK cells. CD8 + T cells are a critical component of the tumor immune response and represent a major target for cancer immunotherapy [57]. We observed significantly lower infiltration of activated CD8 + T cells in the high-risk group than in the low-risk group, suggesting pronounced CD8 + T cell immune escape in the former. Typically, the immunoglobulin-like receptors on NK cells bind to MHC-I molecules on normal cells, inhibiting NK cell cytotoxicity. Tumor cells, however, often lack MHC-I, making them more susceptible to NK-mediated killing [55]. Interestingly, our study revealed decreased NK cell infiltration and cytotoxicity in the high-risk group despite reduced MHC-I activity, suggesting possible inhibition of NK cell activation.

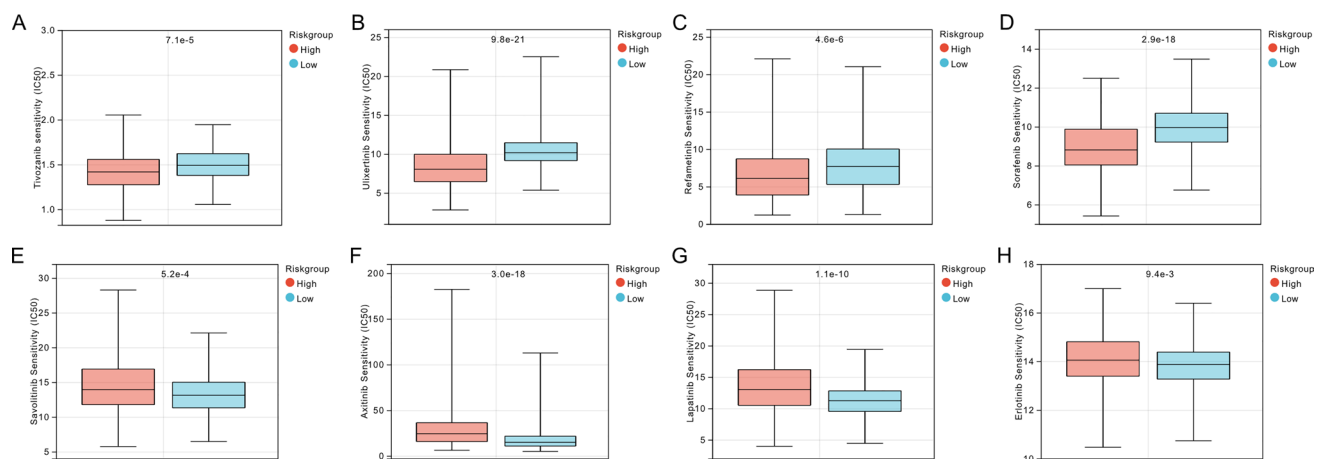


Fig. 9 The predictive value of the FMG-related risk signature in chemotherapy. (A-H) Drug sensitivity analysis between two risk groups

To investigate further, we compared the expression levels of activating receptors DNAM-1 and NKG2D ligand-encoding genes *PVR*, *MICA*, *MICB*, and *ULBP1* in the high-risk and low-risk groups. We found elevated *PVR* expression but reduced *MICA*, *MICB*, and *ULBP1* expression (Fig. S9A). We then compared the expression levels of NK activating receptor-encoding genes *CD226* (DNAM-1), *NCR1*, *NCR2*, *NCR3*, *KLRC1*, and *KLRK1* in both groups, observing lower expression in the high-risk group (Fig. S9B). These findings suggest that an imbalance between NK cell activation and inhibition may underlie the NK cell escaping in the high-risk group. Additionally, *MYCN* amplification, a characteristic genetic alteration in NB, also has a significant impact on the immune microenvironment. For patients without *MYCN* amplification, when stratified based on the FMG-related risk signature, the high-risk group exhibited reduced MHC-I activity compared to the low-risk group. However, the expression levels of activating ligand-encoding genes, such as *MICA* and *ULBP1*, and activating receptor-encoding genes were also lower in the high-risk group (Fig. S9C-D). This suggests that the decreased expression of these activating genes, may lead to diminished NK cell infiltration and function. In contrast, there were no differences in APM or activated CD8 + T cell infiltration levels between the two groups. These findings indicate that, in the absence of strong *MYCN* signaling, the abnormal NK cell function in the high-risk group is a significant issue. Furthermore, *MYCN* may have a more pronounced inhibitory effect on antigen presentation mechanisms and activated CD8 + T cells. In conclusion, the FMG-related risk signature can predict immune cell infiltration in patients, offering insights into the immune landscape of NB and guiding personalized immunotherapy strategies.

The progress in cancer immunotherapy, particularly through the blockade of immune checkpoint pathways, has revolutionized oncological treatments [58, 59]. However, the success of such therapies is highly dependent on the immunogenic properties of the tumor, with some cancers, like NB, presenting unique challenges due to their low mutation burden, low MHC-I expression, and thus reduced immunogenicity [29, 55, 60]. Hence, in the context of clinical management, the effective identification of treatments to which patients are particularly responsive is of paramount importance. Our findings indicate that the expression levels of most immune checkpoint genes are notably higher in the low-risk group. These findings suggest that the responsiveness to immune checkpoint inhibitors may differ between the different risk groups, although this requires further investigation to confirm. Additionally, in patients without *MYCN* amplification, 34 immune checkpoint genes showed differential expression between the high-risk and low-risk groups (Fig. S9E). This is a reduction of 8 genes compared to the differences observed in the entire sample set, specifically *ADORA2A*, *CD44*, *CD80*, *CTLA4*, *PDCD1*, *TIGIT*, *TNFRSF8*, and *VTCN1*. This suggests that *MYCN* may have a more significant impact on the expression of these immune checkpoint genes. Additionally, we have undertaken predictions to delineate chemotherapy drugs that may be efficacious in the low-risk or high-risk groups. Consequently, the FMG-related risk signature bears significant potential in informing the choice of chemotherapeutic agents, thereby contributing to the personalization of cancer therapy.

Furthermore, the results from functional enrichment analysis of DEGs between the two groups provide insights into the molecular mechanisms underlying the differences between high-risk and low-risk groups, suggesting that the high-risk group may have increased metabolic demands and DNA damage response, while the low-risk group may have enhanced signaling and tumor suppression mechanisms. Understanding these pathways can guide future research into therapeutic interventions and personalized medicine strategies for patients in each risk group.

This study, however, does come with some limitations: the expression levels of FMGs in NB cells and patients still need further verification. Moreover, the role of the genes in the risk signature requires further investigation. Additionally, the precise mechanisms leading to immune escape in the high-risk group remain to be explored.

5 Conclusion

In this work, we have developed a novel FMG-related risk signature, achieving precise OS prediction for NB. Moreover, the risk signature identifies distinct immunological landscapes and mechanisms of immune evasion between risk groups, and it can be utilized to predict responses to immunotherapy and pharmacological treatments. This work underscores the pivotal role of fatty acid metabolism in the prognosis and immune microenvironment of NB, potentially offering insights for clinical assessment and therapeutic decision-making.

Acknowledgements None.

Author contributions YQL, SZW and DZ conceived and designed the study. SZW and DZ performed data analysis. MG, NJZ and WY participated in data validation. SZW and DZ prepared the figures and original manuscript. YQL reviewed and edited the manuscript. All authors have read and approved the final manuscript.

Funding This work was supported by “CAMS Innovation Fund for Medical Sciences (CIFMS; 2021-1-I2M-053 to Yuqin Liu)”.

Data availability The datasets analyzed during the current study are available from the corresponding author on reasonable request.

Declarations

Ethics approval and consent to participation This manuscript is not a clinical trial and not involved in animal experiments, hence the ethics approval and consent to participation are not applicable.

Consent for publication Not applicable.

Competing interests The authors declare no competing interests.

Open Access This article is licensed under a Creative Commons Attribution-NonCommercial-NoDerivatives 4.0 International License, which permits any non-commercial use, sharing, distribution and reproduction in any medium or format, as long as you give appropriate credit to the original author(s) and the source, provide a link to the Creative Commons licence, and indicate if you modified the licensed material. You do not have permission under this licence to share adapted material derived from this article or parts of it. The images or other third party material in this article are included in the article's Creative Commons licence, unless indicated otherwise in a credit line to the material. If material is not included in the article's Creative Commons licence and your intended use is not permitted by statutory regulation or exceeds the permitted use, you will need to obtain permission directly from the copyright holder. To view a copy of this licence, visit <http://creativecommons.org/licenses/by-nc-nd/4.0/>.

References

1. Maris JM. Recent advances in neuroblastoma. *N Engl J Med*. 2010;362:2202–11. <https://doi.org/10.1056/NEJMra0804577>.
2. Ni X, Li Z, Li X, Zhang X, Bai G, Liu Y, Zheng R, Zhang Y, Xu X, Liu Y, Jia C, Wang H, Ma X, Zheng H, Su Y, Ge M, Zeng Q, Wang S, Zhao J, Zeng Y, Feng G, Xi Y, Deng Z, Guo Y, Yang Z, Zhang J. Socioeconomic inequalities in cancer incidence and access to health services among children and adolescents in China: a cross-sectional study. *Lancet*. 2022;400:1020–32. [https://doi.org/10.1016/S0140-6736\(22\)01541-0](https://doi.org/10.1016/S0140-6736(22)01541-0).
3. Maris JM, Hogarty MD, Bagatell R, Cohn SL. Neuroblastoma. *Lancet*. 2007;369:2106–20. [https://doi.org/10.1016/S0140-6736\(07\)60983-0](https://doi.org/10.1016/S0140-6736(07)60983-0).
4. Lundberg KI, Treis D, Johnsen JI. Neuroblastoma heterogeneity, plasticity, and emerging therapies. *Curr Oncol Rep*. 2022;24:1053–62. <https://doi.org/10.1007/s11912-022-01270-8>.
5. Spencer B, Patel A, Cilley R, Grant CN. Surgical management in pediatric neuroblastoma diagnosis and treatment: a 20-year, single-center experience. *World J Pediatr*. 2022;18:120–5. <https://doi.org/10.1007/s12519-021-00490-5>.
6. Pinto NR, Applebaum MA, Volchenboum SL, Matthay KK, London WB, Ambros PF, Nakagawara A, Berthold F, Schleiermacher G, Park JR, Valteau-Couanet D, Pearson ADJ, Cohn SL. Advances in risk classification and treatment strategies for neuroblastoma. *J Clin Oncol*. 2015;33:3008–17. <https://doi.org/10.1200/JCO.2014.59.4648>.
7. Whittle SB, Smith V, Doherty E, Zhao S, McCarty S, Zage PE. Overview and recent advances in the treatment of neuroblastoma. *Expert Rev Anticancer Ther*. 2017;17:369–86. <https://doi.org/10.1080/14737140.2017.1285230>.

8. Cui W, Liu D, Gu W, Chu B. Peroxisome-driven ether-linked phospholipids biosynthesis is essential for ferroptosis. *Cell Death Differ.* 2021;28:2536–51. <https://doi.org/10.1038/s41418-021-00769-0>.
9. Chen X, Kang R, Kroemer G, Tang D. Organelle-specific regulation of ferroptosis. *Cell Death Differ.* 2021;28:2843–56. <https://doi.org/10.1038/s41418-021-00859-z>.
10. Tao L, Mohammad MA, Milazzo G, Moreno-Smith M, Patel TD, Zorman B, Badachhape A, Hernandez BE, Wolf AB, Zeng Z, Foster JH, Aloisi S, Sumazin P, Zu Y, Hicks J, Ghaghada KB, Putluri N, Perini G, Coarfa C, Barbieri E. MYCN-driven fatty acid uptake is a metabolic vulnerability in neuroblastoma. *Nat Commun.* 2022;13:3728. <https://doi.org/10.1038/s41467-022-31331-2>.
11. Barnés CM, Prox D, Christison-Lagay EA, Le HD, Short S, Cassiola F, Panigrahy D, Chaponis D, Butterfield C, Nehra D, Fallon EM, Kieran M, Folkman J, Puder M. Inhibition of neuroblastoma cell proliferation with omega-3 fatty acids and treatment of a murine model of human neuroblastoma using a diet enriched with omega-3 fatty acids in combination with sunitinib. *Pediatr Res.* 2012;71:168–78. <https://doi.org/10.1038/pr.2011.28>.
12. Manzo T, Prentice BM, Anderson KG, Raman A, Schalck A, Codreanu GS, Nava Lauson CB, Tiberti S, Raimondi A, Jones MA, Reyzer M. Accumulation of long-chain fatty acids in the tumor microenvironment drives dysfunction in intrapancreatic CD8+ T cells. *J Exp Med.* 2020;217(8):e20191920. <https://doi.org/10.1084/jem.20191920>.
13. Wen XY, Wang RY, Yu B, Yang Y, Yang J, Zhang HC. Integrating single-cell and bulk RNA sequencing to predict prognosis and immunotherapy response in prostate cancer. *Sci Rep.* 2023;13:15597. <https://doi.org/10.1038/s41598-023-42858-9>.
14. Lin H, Fu L, Li P, Zhu J, Xu Q, Wang Y, Mumin MA, Zhou X, Chen Y, Shu G, Yao G, Chen M, Lu J, Zhang L, Liu Y, Zhao Y, Bao J, Chen W, Luo J, Li X, Chen Z, Cao J. Fatty acids metabolism affects the therapeutic effect of anti-PD-1/PD-L1 in tumor immune microenvironment in clear cell renal cell carcinoma. *J Transl Med.* 2023;21:343. <https://doi.org/10.1186/s12967-023-04161-z>.
15. Wilkerson MD, Hayes DN. ConsensusClusterPlus: a class discovery tool with confidence assessments and item tracking. *Bioinformatics.* 2010;26:1572–3. <https://doi.org/10.1093/bioinformatics/btq170>.
16. Shi Y, Wang Y, Dong H, Niu K, Zhang W, Feng K, Yang R, Zhang Y. Crosstalk of ferroptosis regulators and tumor immunity in pancreatic adenocarcinoma: novel perspective to mRNA vaccines and personalized immunotherapy. *Apoptosis.* 2023;28:1423–35. <https://doi.org/10.1007/s10495-023-01868-8>.
17. Wang P, Wang Y, Hang B, Zou X, Mao J-H. A novel gene expression-based prognostic scoring system to predict survival in gastric cancer. *Oncotarget.* 2016;7:55343–51. <https://doi.org/10.18632/oncotarget.10533>.
18. Friedman J, Hastie T, Tibshirani R, Narasimhan B, Tay K, Simon N, Qian J, Yang J. glmnet: Lasso and elastic-net regularized generalized linear models. *Astrophysics Source Code Library.* 2023. <https://doi.org/10.32614/CRAN.package.glmnet>.
19. Robin X, Turck N, Hainard A, Tiberti N, Lisacek F, Sanchez J-C, Müller M. pROC: an open-source package for R and S+ to analyze and compare ROC curves. *BMC Bioinformatics.* 2011;12:77. <https://doi.org/10.1186/1471-2105-12-77>.
20. Sun D, Tian L, Zhu Y, Wo Y, Liu Q, Liu S, Li H, Hou H. Subunits of ARID1 serve as novel biomarkers for the sensitivity to immune checkpoint inhibitors and prognosis of advanced non-small cell lung cancer. *Mol Med.* 2020;26:78. <https://doi.org/10.1186/s10020-020-00208-9>.
21. Hänzelmann S, Castelo R, Guinney J. GSEA: gene set variation analysis for microarray and RNA-seq data. *BMC Bioinformatics.* 2013;14:7. <https://doi.org/10.1186/1471-2105-14-7>.
22. Yang J, Han L, Sha Y, Jin Y, Li Z, Gong B, Li J, Liu Y, Wang Y, Zhao Q. A novel ganglioside-related risk signature can reveal the distinct immune landscape of neuroblastoma and predict the immunotherapeutic response. *Front Immunol.* 2022;13:1061814. <https://doi.org/10.3389/fimmu.2022.1061814>.
23. Yoshihara K, Shahmoradgol M, Martínez E, Vegesna R, Kim H, Torres-Garcia W, Treviño V, Shen H, Laird PW, Levine DA, Carter SL, Getz G, Stemke-Hale K, Mills GB, Verhaak RGW. Inferring tumour purity and stromal and immune cell admixture from expression data. *Nat Commun.* 2013;4:2612. <https://doi.org/10.1038/ncomms3612>.
24. Maeser D, Gruener RF, Huang RS. oncoPredict: an R package for predicting in vivo or cancer patient drug response and biomarkers from cell line screening data. *Brief Bioinformatics.* 2021;22(6):bbab260. <https://doi.org/10.1093/bib/bbab260>.
25. Yang H, Yang J, Bian H, Wang X. A novel cuproptosis-related gene signature predicting overall survival in pediatric neuroblastoma patients. *Front Pediatr.* 2022;10:1049858. <https://doi.org/10.3389/fped.2022.1049858>.
26. Smyth GK. Linear models and empirical Bayes methods for assessing differential expression in microarray experiments. *Stat Appl Genet Mol Biol.* 2004;3:3. <https://doi.org/10.2202/1544-6115.1027>.
27. Yu G, Wang L-G, Han Y, He Q-Y. clusterProfiler: an R package for comparing biological themes among gene clusters. *OMICS.* 2012;16:284–7. <https://doi.org/10.1089/omi.2011.0118>.
28. Szklarczyk D, Kirsch R, Koutrouli M, Nastou K, Mehryary F, Hachilif R, Gable AL, Fang T, Doncheva NT, Pyysalo S, Bork P, Jensen LJ, von Mering C. protein-protein association networks and functional enrichment analyses for any sequenced genome of interest. *Nucleic Acids Res.* 2023;51(2023):D638–46. <https://doi.org/10.1093/nar/gkac1000>.
29. Anderson J, Majzner RG, Sondel PM. Immunotherapy of neuroblastoma: facts and hopes. *Clin Cancer Res.* 2022;28:3196–206. <https://doi.org/10.1158/1078-0432.CCR-21-1356>.
30. Verhoeven BM, Mei S, Olsen TK, Gustafsson K, Valind A, Lindström A, Gisselsson D, Fard SS, Hagerling C, Kharchenko PV, Kogner P, Johnsen JJ, Baryawno N. The immune cell atlas of human neuroblastoma. *Cell Rep Med.* 2022;3: 100657. <https://doi.org/10.1016/j.xcrm.2022.100657>.
31. Qiu B, Matthay KK. Advancing therapy for neuroblastoma. *Nat Rev Clin Oncol.* 2022;19:515–33. <https://doi.org/10.1038/s41571-022-00643-z>.
32. Lin Y, Meng Y, Zhang J, Ma L, Jiang L, Zhang Y, Yuan M, Ren A, Zhu W, Li S, Shu Y, Du M, Zhu L. Functional genetic variant of HSD17B12 in the fatty acid biosynthesis pathway predicts the outcome of colorectal cancer. *J Cell Mol Med.* 2020;24:14160–70. <https://doi.org/10.1111/jcmm.16026>.
33. Zhang Z, Zou Y, Zhu J, Zhang R, Yang T, Wang F, Xia H, He J, Feng Z. HSD17B12 gene rs11037575 C>T polymorphism confers neuroblastoma susceptibility in a Southern Chinese population. *Onco Targets Ther.* 2017;10:1969–75. <https://doi.org/10.2147/OTT.S136006>.
34. Zhang S, Yang Y, Shi Y. Characterization of human SCD2, an oligomeric desaturase with improved stability and enzyme activity by cross-linking in intact cells. *Biochem J.* 2005;388:135–42. <https://doi.org/10.1042/BJ20041554>.

35. Tesfay L, Paul BT, Konstorum A, Deng Z, Cox AO, Lee J, Furdul CM, Hegde P, Torti FM, Torti SV. Stearoyl-CoA desaturase 1 protects ovarian cancer cells from ferroptotic cell death. *Cancer Res.* 2019;79:5355–66. <https://doi.org/10.1158/0008-5472.CAN-19-0369>.
36. Luis G, Godfroid A, Nishiumi S, Cimino J, Blacher S, Maquoi E, Wery C, Collignon A, Longuespée R, Montero-Ruiz L, Dassoul I, Maloujahmoum N, Pottier C, Mazzucchelli G, Depauw E, Bellahcène A, Yoshida M, Noel A, Sounni NE. Tumor resistance to ferroptosis driven by Stearoyl-CoA Desaturase-1 (SCD1) in cancer cells and Fatty Acid Binding Protein-4 (FABP4) in tumor microenvironment promote tumor recurrence. *Redox Biol.* 2021;43: 102006. <https://doi.org/10.1016/j.redox.2021.102006>.
37. Zhao R, Tian L, Zhao B, Sun Y, Cao J, Chen K, Li F, Li M, Shang D, Liu M. FADS1 promotes the progression of laryngeal squamous cell carcinoma through activating AKT/mTOR signaling. *Cell Death Dis.* 2020;11:272. <https://doi.org/10.1038/s41419-020-2457-5>.
38. Lee J-Y, Nam M, Son HY, Hyun K, Jang SY, Kim JW, Kim MW, Jung Y, Jang E, Yoon S-J, Kim J, Kim J, Seo J, Min J-K, Oh K-J, Han B-S, Kim WK, Bae K-H, Song J, Kim J, Huh Y-M, Hwang G-S, Lee E-W, Lee SC. Polyunsaturated fatty acid biosynthesis pathway determines ferroptosis sensitivity in gastric cancer. *Proc Natl Acad Sci U S A.* 2020;117:32433–42. <https://doi.org/10.1073/pnas.2006828117>.
39. Moon Y-A, Horton JD. Identification of two mammalian reductases involved in the two-carbon fatty acyl elongation cascade. *J Biol Chem.* 2003;278:7335–43. <https://doi.org/10.1074/jbc.M211684200>.
40. Su Y-C, Feng Y-H, Wu H-T, Huang Y-S, Tung C-L, Wu P, Chang C-J, Shiau A-L, Wu C-L. Elov16 is a negative clinical predictor for liver cancer and knockdown of Elov16 reduces murine liver cancer progression. *Sci Rep.* 2018;8:6586. <https://doi.org/10.1038/s41598-018-24633-3>.
41. McAndrew RP, Wang Y, Mohsen A-W, He M, Vockley J, Kim J-JP. Structural basis for substrate fatty acyl chain specificity: crystal structure of human very-long-chain acyl-CoA dehydrogenase. *J Biol Chem.* 2008;283:9435–43. <https://doi.org/10.1074/jbc.M709135200>.
42. Tcheng M, Roma A, Ahmed N, Smith RW, Jayanth P, Minden MD, Schimmer AD, Hess DA, Hope K, Rea KA, Akhtar TA, Bohrsen E, D'Alessandro A, Mohsen A-W, Vockley J, Spagnuolo PA. Very long chain fatty acid metabolism is required in acute myeloid leukemia. *Blood.* 2021;137:3518–32. <https://doi.org/10.1182/blood.202008551>.
43. Zhou Q, Tian W, Jiang Z, Huang T, Ge C, Liu T, Zhao F, Chen T, Cui Y, Li H, Yao M, Li J, Tian H. A positive feedback loop of AKR1C3-mediated activation of NF- κ B and STAT3 facilitates proliferation and metastasis in hepatocellular carcinoma. *Cancer Res.* 2021;81:1361–74. <https://doi.org/10.1158/0008-5472.CAN-20-2480>.
44. Lyon RC, Li D, McGarvie G, Ellis EM. Aldo-keto reductases mediate constitutive and inducible protection against aldehyde toxicity in human neuroblastoma SH-SY5Y cells. *Neurochem Int.* 2013;62:113–21. <https://doi.org/10.1016/j.neuint.2012.10.007>.
45. Kanaoka Y, Fujimori K, Kikuno R, Sakaguchi Y, Urade Y, Hayaishi O. Structure and chromosomal localization of human and mouse genes for hemopoietic prostaglandin D synthase. Conservation of the ancestral genomic structure of sigma-class glutathione S-transferase. *Eur J Biochem.* 2000;267:3315–22. <https://doi.org/10.1046/j.1432-1327.2000.01362.x>.
46. Xie Z, Niu L, Zheng G, Du K, Dai S, Li R, Dan H, Duan L, Wu H, Ren G, Dou X, Feng F, Zhang J, Zheng J. Single-cell analysis unveils activation of mast cells in colorectal cancer microenvironment. *Cell Biosci.* 2023;13:217. <https://doi.org/10.1186/s13578-023-01144-x>.
47. Jiang Y, Qu X, Zhang M, Zhang L, Yang T, Ma M, Jing M, Zhang N, Song R, Zhang Y, Yang Z, Zhang Y, Pu Y, Fan J. Identification of a six-gene prognostic signature for bladder cancer associated macrophage. *Front Immunol.* 2022;13: 930352. <https://doi.org/10.3389/fimmu.2022.930352>.
48. Morgan RA, Beck KR, Nixon M, Homer NZM, Crawford AA, Melchers D, Houtman R, Meijer OC, Stomby A, Anderson AJ, Upreti R, Stimson RH, Olsson T, Michael T, Cohain A, Ruusalepp A, Schadt EE, Björkegren JLM, Andrew R, Kenyon CJ, Hadoke PWF, Odermatt A, Keen JA, Walker BR. Carbonyl reductase 1 catalyzes 20 β -reduction of glucocorticoids, modulating receptor activation and metabolic complications of obesity. *Sci Rep.* 2017;7:10633. <https://doi.org/10.1038/s41598-017-10410-1>.
49. Zhou L, Yang C, Zhong W, Wang Q, Zhang D, Zhang J, Xie S, Xu M. Chrysin induces autophagy-dependent ferroptosis to increase chemosensitivity to gemcitabine by targeting CBR1 in pancreatic cancer cells. *Biochem Pharmacol.* 2021;193: 114813. <https://doi.org/10.1016/j.bcp.2021.114813>.
50. Przybyla-Zawislak BD, Srivastava PK, Vazquez-Matias J, Mohrenweiser HW, Maxwell JE, Hammock BD, Bradbury JA, Enayetallah AE, Zeldin DC, Grant DF. Polymorphisms in human soluble epoxide hydrolase. *Mol Pharmacol.* 2003;64:482–90. <https://doi.org/10.1124/mol.64.2.482>.
51. Newman JW, Morisseau C, Harris TR, Hammock BD. The soluble epoxide hydrolase encoded by EPXH2 is a bifunctional enzyme with novel lipid phosphate phosphatase activity. *Proc Natl Acad Sci U S A.* 2003;100:1558–63. <https://doi.org/10.1073/pnas.0437724100>.
52. Liu M-S, Zhao H, Xu C-X, Xie P-B, Wang W, Yang Y-Y, Lee W-H, Jin Y, Zhou H-Q. Clinical significance of EPHX2 deregulation in prostate cancer. *Asian J Androl.* 2021;23:109–15. https://doi.org/10.4103/aja.aja_34_20.
53. Zhou Y, Li X, Guan A, Zhou H, Zhu Y, Wang R, Li R. EPHX2 inhibits colon cancer progression by promoting fatty acid degradation. *Front Oncol.* 2022;12: 870721. <https://doi.org/10.3389/fonc.2022.870721>.
54. Zhan K, Bai Y, Liao S, Chen H, Kuang L, Luo Q, Lv L, Qiu L, Mei Z. Identification and validation of EPHX2 as a prognostic biomarker in hepatocellular carcinoma. *Mol Med Rep.* 2021;24:650. <https://doi.org/10.3892/mmr.2021.12289>.
55. Wienke J, Dierselhuis MP, Tytgat GAM, Künkele A, Nierkens S, Molenaar JJ. The immune landscape of neuroblastoma: challenges and opportunities for novel therapeutic strategies in pediatric oncology. *Eur J Cancer.* 2021;144:123–50. <https://doi.org/10.1016/j.ejca.2020.11.014>.
56. Jiménez C, Moreno L, Segura MF. Epigenetic therapies for neuroblastoma: immunogenicity awakens. *Mol Oncol.* 2023;17:718–21. <https://doi.org/10.1002/1878-0261.13404>.
57. Durgeau A, Virk Y, Corgnac S, Mami-Chouaib F. Recent advances in targeting CD8 T-cell immunity for more effective cancer immunotherapy. *Front Immunol.* 2018;9:14. <https://doi.org/10.3389/fimmu.2018.00014>.
58. Zhang Y, Zhang Z. The history and advances in cancer immunotherapy: understanding the characteristics of tumor-infiltrating immune cells and their therapeutic implications. *Cell Mol Immunol.* 2020;17:807–21. <https://doi.org/10.1038/s41423-020-0488-6>.
59. Riley RS, June CH, Langer R, Mitchell MJ. Delivery technologies for cancer immunotherapy. *Nat Rev Drug Discov.* 2019;18:175–96. <https://doi.org/10.1038/s41573-018-0006-z>.
60. Bagchi S, Yuan R, Engleman EG. Immune checkpoint inhibitors for the treatment of cancer: clinical impact and mechanisms of response and resistance. *Annu Rev Pathol.* 2021;16:223–49. <https://doi.org/10.1146/annurev-pathol-042020-042741>.